

ANALYSIS OF MEASURED POST-COUPLER FIELDS IN A RAMPED-GRADIENT DRIFT-TUBE LINAC\*

James H. Billen

Los Alamos National Laboratory, MS H817, Los Alamos, NM 87545

Abstract

Post couplers longitudinally stabilize the axial electric field in a drift-tube linac (DTL) against tuning errors. Displacing the post couplers toward one end of the structure results in a ramped field that increases toward the other end. Such a ramped-gradient DTL is also stable, but some of the cavity power is dissipated on the post couplers to maintain the ramp. This paper reports bead-perturbation measurements of the post-coupler magnetic fields near the tank wall. A simple physical model reproduces the measured fields with an accuracy of about 2% and yields current-density distributions on the post couplers in terms of the current density on the cavity wall. The peak power density occurs on the sides of the post couplers where the  $TM_{010}$  magnetic field adds to the post-coupler magnetic field. In the Los Alamos Ramped-Gradient DTL (RGDTL), the peak power densities on post couplers located in the steepest part of the ramp exceed by more than 10 times the maximum power density on the tank wall far from any post couplers. Methods to reduce such power losses to levels comparable to a flat-gradient DTL will be discussed.

Introduction

The Los Alamos RGDTL is a 425-MHz, 30-cell structure equipped with 14 post couplers. A companion paper<sup>1</sup> discusses the low-power rf tuning of the RGDTL, and another paper<sup>2</sup> describes features of its mechanical design. As mentioned in Ref. 1, the post couplers in the RGDTL must carry current and, hence, dissipate power in order to maintain the ramped-field distribution. A measurement of the magnetic field near the cavity wall quantifies the post-coupler power densities in terms of the power density corresponding to the  $TM_{010}$  fields.

Magnetic-Field Measurements

To measure a longitudinal field distribution near the cavity wall, we use the bead-perturbation technique. A metallic sphere supported on a nylon line and pulled through the cavity at constant speed continually shifts the cavity frequency by an amount proportional to the magnetic field stored energy displaced by the bead. The 1-cm-diam, hollow, aluminum bead used for these measurements has a mass of 0.34 g. With ~22-N tension in the nylon line, the bead causes less than 0.01-cm sag in the line. Figures 1 and 2 show end and side views of the bead trajectory relative to the post-coupler positions. Our data acquisition program BEADPULL samples the frequency shift 9900 times during the 20 s it takes the bead to traverse the cavity.

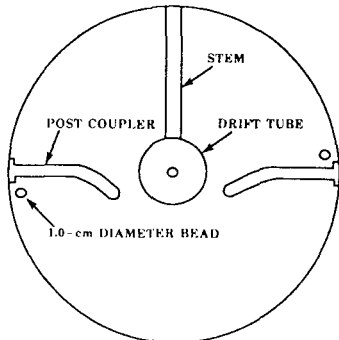


Fig. 1. Sketch of the RGDTL viewed from the end, showing the location of the bead relative to the post couplers for magnetic field measurements.

\* Work supported and funded by the US Department of Defense, Army Strategic Defense Command, under the auspices of the US Department of Energy.

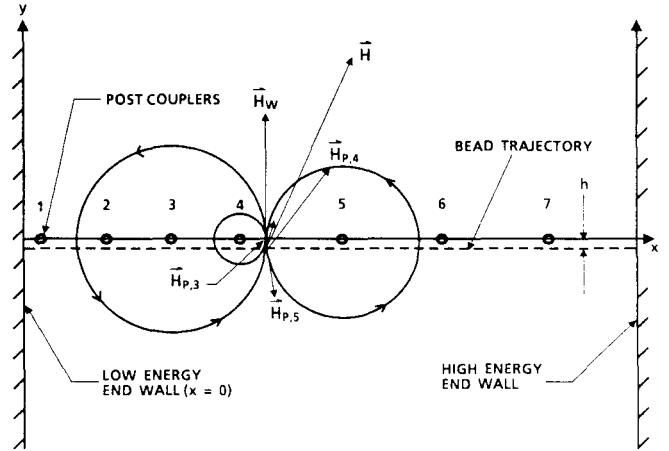


Fig. 2. Side view of the bead trajectory relative to the post-coupler locations. Circles around three of the post couplers show the magnetic field direction for a positive current on the post coupler (flowing out of the page).

The resultant field  $\vec{H}$  is the vector addition of the  $TM_{010}$  field  $\vec{H}_W$  and contributions from all seven post-coupler fields  $H_{P,j}$ . Only the three nearest  $H_{P,j}$  are shown here.

Figure 3 shows a typical measurement for the bead along-side the seven post couplers on the right side of the RGDTL viewed from the low-energy (LE) end. Zero frequency shift corresponds to the bead completely outside the cavity. A negative frequency shift means that the signal generator's reference frequency is low compared to the cavity frequency. The metal bead lowers inductance by displacing magnetic field and, hence, raises the cavity frequency. The shift measured in kilohertz is proportional to the square of the magnetic field.

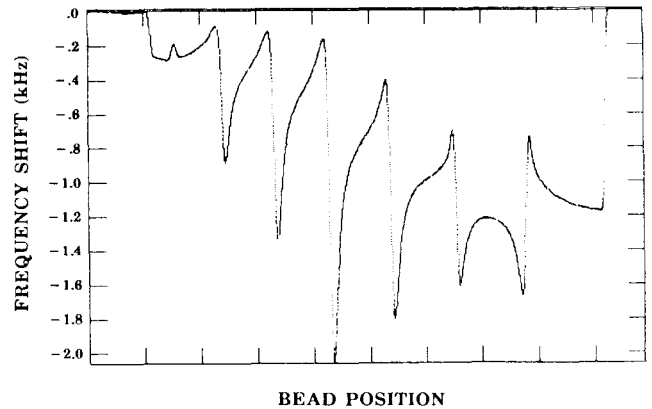


Fig. 3. Bead-perturbation data for a magnetic field measurement near the seven post couplers on the right-hand side of the RGDTL viewed from the low-energy end.

Analysis

Figure 2 defines a rectangular coordinate system in which all the post couplers on one side of the tank are located at  $y = 0$ . When the bead is at position  $(x, y)$  along the trajectory, the observed frequency shift  $\Delta f$  is proportional to the absolute square of the resultant magnetic field:

$$\Delta f = k|\vec{H}(x, y)|^2 = |\vec{H}_W(x, y) + \sum_{j=1}^7 \vec{H}_{P,j}(x, y)|^2, \quad (1)$$

where  $k$  is a constant of proportionality,  $\vec{H}_W$  is the  $TM_{010}$  component of the magnetic field near the wall, and  $\vec{H}_{P,j}$  is the magnetic field associated with current flow on the  $j$ th post coupler. Far from any of the post couplers, the field  $\vec{H}_W$  is in the positive  $y$  direction, but it distorts to go around a cylindrical (conducting) obstruction such as a post coupler. This distortion can be included in  $\vec{H}_W$  by the addition of a dipole field centered on the cylinder. The strength of the dipole term must satisfy the boundary condition that the perpendicular component of the total field vanish on the cylindrical surface. In terms of the rectangular coordinates of Fig. 2:

$$\vec{H}_W(x, y) = H_R(x)\hat{y} + \sum_{j=1}^7 \frac{R_P^3 H_R(x_j)}{2r_j^3} \left[ -\frac{3y(x-x_j)}{r_j^2} \hat{x} + \left( 1 - \frac{3y^2}{r_j^2} \right) \hat{y} \right] \quad (2)$$

where  $H_R(x)$  is the smoothly varying magnitude of the ramped magnetic field for the  $TM_{010}$  mode of the cavity,  $R_P$  is the radius of the post coupler,  $\hat{x}$  and  $\hat{y}$  are unit vectors in the  $+x$  and  $+y$  directions, respectively, and

$$r_j = \left[ (x-x_j)^2 + y^2 \right]^{1/2} \quad (3)$$

The summations in Eqs. (1) and (2) are over the contribution to the resultant field from all seven post couplers on one side of the tank. The post coupler magnetic fields arise from current flowing along the post couplers and vary as  $1/r_j$ , where  $r_j$  is the distance from the center of the  $j$ th post coupler. The magnetic field for the  $j$ th post coupler field is

$$\vec{H}_{P,j}(x, y) = \frac{I_j}{2\pi r_j^2} [-y\hat{x} + (x-x_j)\hat{y}] \quad (4)$$

where  $I_j$  is the current flowing on the  $j$ th post coupler.

The task of fitting Eqs. (1) through (4) to the measured data requires a nonlinear fitting procedure because the observable quantity is a frequency shift proportional to the square of  $\vec{H}$ . I used a nonlinear least-squares, variable-metric fitting routine to determine a total of 17 parameters for a given measurement. The parameters are seven post-coupler currents  $I_j$ , six coefficients of a fifth-order polynomial in  $x$  to describe  $H_R$ , two parameters that locate the ends of the rf structure within the data array, the distance  $h$  (see Fig. 2) of the bead trajectory from the post-coupler centers, and the effective diameter of the post couplers near the wall of the cavity. The post-coupler locations with respect to the end walls of the rf structure are not adjustable parameters.

The effective post-coupler diameter is a free parameter because of a change in diameter of the post couplers near the tank wall. The diameter changes from 2.05 to 1.27 cm at about 0.7 cm from the tank wall for most of the post couplers (see Fig. 1). Because the bead passes so close to the change in diameter, it samples a mixture of dipole field components associated with both post-coupler diameters. The fitting procedure finds an effective diameter of  $1.80 \pm 0.06$  cm, which is in between the two post-coupler diameters near the bead trajectory.

The distance  $h$  is also a free parameter. The fitting function is sensitive to smaller changes in the parameter  $h$  than the accuracy with which  $h$  is known from mechanical measurements. The nominal values are  $-1.588$  cm for measurements on one side of the tank and  $+1.588$  cm on the other side. The fitted distances are  $-1.627 \pm 0.017$  cm and  $1.597 \pm 0.025$  cm. Differences are within the mechanical alignment errors allowed by the size of the bolt holes in the end plates and by alignment of the bead with respect to the centers of the holes through which the bead passes.

## Results

Figure 4 shows a typical fit, this one for data taken near the seven post couplers on the right-hand side of the RGDTL

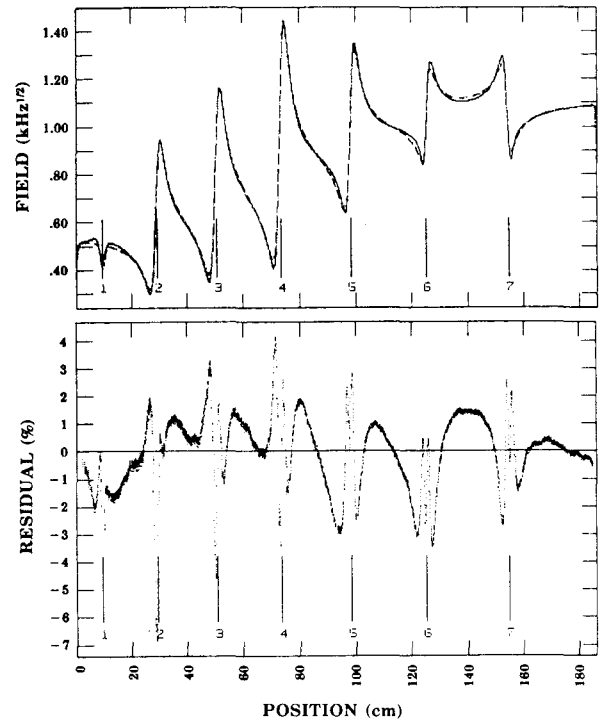


Fig. 4. Fitted results for the measurement of Fig. 3. The numbered markers indicate post-coupler locations. Upper plot shows the data and a fitted curve. Lower plot shows the fit minus data as a percentage of  $H_{MAX}$ . Overall rms error for case was 1.37% of  $H_{MAX}$ .

viewed from its LE end. These post couplers, at positions 1 through 7 in Fig. 4, penetrate the tank wall at the longitudinal centers of drift tubes 2, 6, 10, 14, 18, 22, and 26, respectively. (The remaining seven post couplers are on the other side of the tank.) The upper plot shows the data consisting of some 8100 points plus a dashed curve fitted to Eqs. (1) through (4). The bottom plot shows the difference between the fitted and the measured field strength as a percentage of  $H_{MAX}$ , the maximum  $TM_{010}$  magnetic field near the tank wall (which occurs near the high-energy end of the tank). The root-mean-square error for this case was 1.37% of  $H_{MAX}$ . Only a few regions are fit with errors larger than 5%.

Table I summarizes the fitted results for six separate measurements, three measurements each near the post couplers on either side of the tank. One of the three measurements corresponds to the nominal, unperturbed ramped field distribution.

TABLE I. MAGNETIC FIELDS<sup>a</sup> CIRCULATING THE POST COUPLERS NEAR THE TANK WALL.

Post-Coupler Number	Drift-Tube Number	-100 kHz No End-cell Perturbation	-100 kHz End-cell Perturbation	+100kHz End-cell Perturbation
1	2	-0.010±0.113	0.666±0.273	-0.621±0.090
2	4	1.307±0.059	1.793±0.072	0.671±0.074
3	6	1.584±0.093	1.927±0.077	1.134±0.109
4	8	2.242±0.074	2.694±0.097	1.590±0.077
5	10	1.982±0.060	2.419±0.060	1.457±0.057
6	12	2.590±0.093	3.061±0.111	1.950±0.080
7	14	2.524±0.059	2.950±0.080	2.019±0.066
8	16	2.320±0.108	2.676±0.124	1.838±0.096
9	18	1.714±0.087	2.139±0.079	1.309±0.103
10	20	1.701±0.106	2.046±0.103	1.255±0.127
11	22	0.920±0.139	1.388±0.131	0.480±0.158
12	24	-0.235±0.098	0.265±0.101	-0.673±0.093
13	26	-0.882±0.098	-0.396±0.128	-1.340±0.078
14	28	-0.729±0.106	-0.386±0.154	-1.038±0.104

<sup>a</sup>Fields and uncertainties are expressed relative to  $H_{MAX}$ , the maximum  $TM_{010}$  magnetic field near the tank wall. These are the fields near the 0.5-in.-diam post coupler arising only from the post-coupler excitation and do not include the  $TM_{010}$  field contribution.

The other two measurements correspond to attempts to disturb the field distribution by deliberately detuning the two end cells of the structure. (See the discussion of tilt sensitivity in Ref. 1.) The table lists the magnetic field strength (in units of  $H_{MAX}$ ) at the surface of the post coupler arising only from current flow along the post coupler.

The resultant magnetic field strength near a post coupler varies with angle around the post-coupler shaft because of the contribution of the local  $TM_{010}$  magnetic field. Figure 5 shows this dependence for post coupler 6 (next to drift tube 12) in the steepest part of the ramped field, and Fig. 6 shows similar data for post coupler 13 (next to drift tube 26) in the unramped portion of the tank. These plots show only the field's magnitude without regard to its direction. The solid curves correspond to no end-cell perturbation of the cavity. The dotted and dashed curves correspond to  $-100$ -kHz and  $+100$ -kHz end-cell perturbations, respectively. Zero degrees is in the direction of positive  $x$  (see Fig. 2), which is toward the high-energy (HE) end of the tank. Similarly,  $180^\circ$  is the LE side of a post coupler. The magnitude of the field is symmetric top to bottom, that is, about  $y = 0$ . The field strengths are in units of  $H_{MAX}$ .

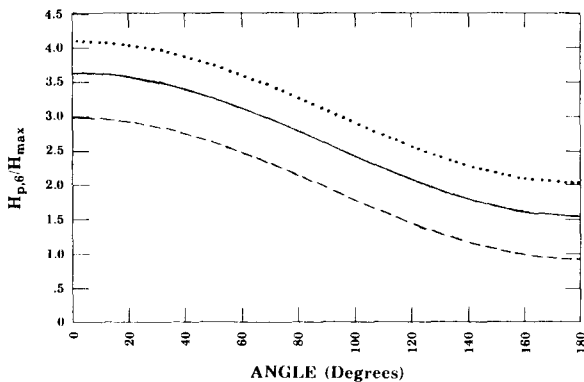


Fig. 5. Resultant azimuthal magnetic field distribution around post coupler 6 (located in the steepest part of the ramped field). Zero degrees and  $180^\circ$  face the high-energy and low-energy ends, respectively. Solid line corresponds to no end-cell perturbation. Dotted and dashed lines correspond to  $-100$ -kHz and  $+100$ -kHz end-cell perturbations.

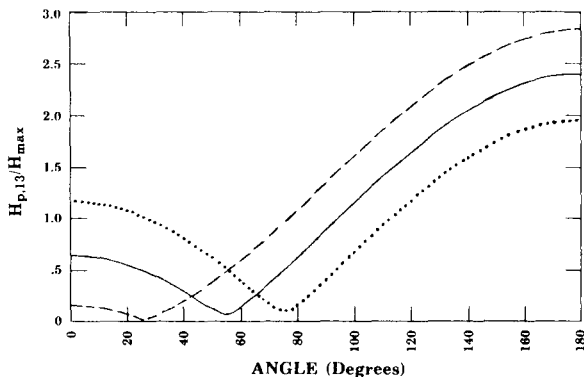


Fig. 6. Resultant azimuthal magnetic field distribution around post coupler 13 (located in a constant-gradient region of the RGDTL). Zero degrees and  $180^\circ$  face the high-energy and low-energy ends, respectively. Solid line corresponds to no end-cell perturbation. Dotted and dashed lines correspond to  $-100$ -kHz and  $+100$ -kHz end-cell perturbations.

The largest magnetic fields occur on the HE side of post couplers in the ramped-field part of the cavity. For the unperturbed cavity, these fields exceed  $3.5 H_{MAX}$  for post couplers 6, 7, and 8, and correspond to local power densities 12 to 13 times the highest power density on the tank wall, far from any post coupler. Post coupler 1 is immersed in the lowest  $TM_{010}$  field, and it also is the least excited of the post couplers. Thus,

post coupler 1 has a peak field of only  $0.8 H_{MAX}$ . The three post couplers on the HE end of the RGDTL (12, 13, and 14) have their highest field at an azimuth angle of  $180^\circ$  (on the LE side). The field circulates in the opposite direction around these three post couplers compared to the others (see Table I) and, therefore, tilts the field locally toward the LE end. Without post couplers, the field ramps slightly toward the HE end because of the drift-tube stems (see Ref. 1). The RGDTL design calls for a short section of constant accelerating gradient near the HE end, so post couplers 12, 13, and 14 actually must shift field toward the LE end. Peak fields near these post couplers are large, even though the contributions from post-coupler currents alone are less than  $H_{MAX}$ . Post coupler 12 is the least excited of the three with a circulating field of  $0.235 H_{MAX}$ , and yet it has a peak magnetic field strength of  $1.7 H_{MAX}$  on its LE side.

The axial field distribution in the RGDTL does not change as a result of end-cell perturbations, nor does the distribution of  $TM_{010}$  magnetic field. However, the post-coupler excitations change almost uniformly (see Table I), counteracting the attempt to superimpose a linear tilt on the field distribution. The  $-100$ -kHz end-cell perturbation attempts to tilt the field toward the LE end. The circulating field around all 14 post couplers changes in the positive sense (see Fig. 2) by  $0.444 \pm 0.088 H_{MAX}$ . Similarly, a  $+100$ -kHz end-cell perturbation causes an opposite-sense change in the post coupler fields of  $-0.500 \pm 0.102 H_{MAX}$ . The relative spacings among the three curves in each of Figs. 5 and 6 also illustrate this effect.

These measurements suggest a method for designing future ramped-gradient DTLs that minimizes the power losses on post couplers. Consider post couplers 2 through 11, which are in the ramped portion of the field. For these 10 post couplers, the  $+100$ -kHz perturbation reduced the circulating fields an average of 30%. Because the effect on the field tilt is approximately linear with end-cell perturbation, a  $+330$ -kHz perturbation would greatly reduce net current flow on these post couplers. In fact, if the ramp itself were linear to begin with (it actually has a cubic shape in the RGDTL), the end-cell detuning would practically eliminate altogether the circulating post-coupler fields, leaving only eddy current losses from the  $TM_{010}$  fields on the post couplers. Measurements of relative stored-energy distributions in a constant-velocity model of a DTL confirm this picture. For fields ramped linearly by end-cell perturbations, the post-coupler excitations can be reduced to the level of ordinary flat-gradient DTLs. In other words, these nominally unexcited post couplers stabilize the *natural* ramp in the field produced by the end-cell perturbations. Other perturbations that tend to disturb the natural distribution excite the post couplers as necessary to prevent the field disturbance.

This method of detuning only the two end cells to reduce post-coupler excitations lends itself to DTLs with a linear ramp. In the case of the RGDTL with its more complicated cubic ramp plus a flat-gradient section, this approach does not work. The  $+100$ -kHz perturbation actually doubled the average circulating fields around post couplers 1, 12, 13, and 14, offsetting much of the reduction discussed above.

## Conclusion

I have described a measurement and analysis procedure for obtaining post-coupler magnetic fields in DTL cavities. For the RGDTL, the post-coupler excitations are large. Future ramped-gradient DTLs can be designed to minimize post-coupler power by deliberately detuning the end cells for a natural linearly ramped field.

## References

1. J. H. Billen and A. H. Shapiro, "Post-Coupler Stabilization and Tuning of a Ramped-Gradient Drift-Tube Linac," these proceedings.
2. D. Liska et al., "A High-Intensity Drift-Tube Linac with Ramped Accelerating Gradient," these proceedings.